

We are IntechOpen, the world's leading publisher of Open Access books Built by scientists, for scientists

6,900

Open access books available

186,000

International authors and editors

200M

Downloads

Our authors are among the

154

Countries delivered to

TOP 1%

most cited scientists

12.2%

Contributors from top 500 universities



WEB OF SCIENCE™

Selection of our books indexed in the Book Citation Index
in Web of Science™ Core Collection (BKCI)

Interested in publishing with us?
Contact book.department@intechopen.com

Numbers displayed above are based on latest data collected.
For more information visit www.intechopen.com



TBL-Induced Structural Vibration and Noise

Zhang Xilong, Kou YiWei and Liu Bilong

Abstract

One of most import noise sources in a jet powered aircraft is turbulent boundary layer (TBL) induced structural vibration. In this chapter, the general model for the prediction of TBL-induced plate vibration and noise is described in detail. Then numerical examples for a typical plate are illustrated. Comparisons of plate vibration and radiated noise between numerical results and wind tunnel test are presented. The effects of structural parameters on modal-averaged radiation efficiency and therefore the radiated noise are discussed. The result indicates that an increment of flow velocity will increase the acoustic radiation efficiency below the hydrodynamic coincidence frequency range. The main reason for this phenomenon is that a higher convection velocity will coincide with lower order modes which have higher radiation efficiencies.

Keywords: turbulent boundary layer, plate vibration, radiated noise, modal radiation efficiency

1. Introduction

The interior noise level in a jet aircraft is mainly depend on noise which generated by turbulent boundary layers (TBL), if the rest of noise sources such as ventilation systems, fans, hydraulic systems, etc. have been appropriately acoustically treated. When the aircraft passes through the atmosphere, the turbulent boundary layer creates pressure fluctuations on the fuselage. These pressure fluctuations cause the aircraft fuselage to vibrate. The noise generated by the vibration is then transmitted to the cabin.

The noise emitted by the aircraft fuselage depends on the speed of the vibrating plate, which in turn depends on the speed of the aircraft, the geometry and size of the plates, and the loss or damping of the plates. It is obvious that the acoustic performances of the internal system, trim panels etc., will also affect the noise inside the aircraft. Graham [1] came up with a model in aircraft plates to predict TBL induced noise, in which the modal excitation terms were calculated by an analytical expression. In Graham's another research [2], the advantages of various models describing the cross power spectral density induced by a flow or TBL across a structure was discussed. Han et al. [3] tried to use energy flow analysis to predict the noise induced by TBL. The method can better predict the response caused by the TBL excitation. However, the noise radiation caused by the flat panel cannot be predicted well. To avoid this deficiency, Liu et al. [4–6] described a model to predict TBL induced noise for aircraft plates. In their work, the modal excitation terms and

acoustical radiation efficiency can be predicted properly and the predicted results are also compared with that of the wind tunnel and in-flight test. Rocha and Palumbo [7] further investigated the sensitivity of sound power radiated by aircraft panels to TBL parameters, and discussed the findings by Liu [4] that ring stiffeners may increase TBL induced noise radiation significantly.

The radiation efficiency of a plate plays an important role in vibro-acoustic problems. In recent related research, the sound medium around the fuselage of the aircraft is often considered to be stationary. Under this assumption, Cremer and Heckl [8] used a more concise formula to predict the acoustic radiation efficiency of an infinite plate. Wallace [9] derived an integral formula based on far-field acoustic radiation power to calculate the modal acoustic radiation efficiency of a finite plate. Kou et al. [10] proposed modifications to the classical formulas given by Cremer and Leppington, regarding the influence of structural damping on the radiation efficiency.

A comparison of the acoustic radiation of the plate with stationary fluid and convective fluid-loaded can be found in [11–13]. Graham [11] and Frampton [12] studied the influence of the mean flow on the modal radiation efficiency of a rectangular plate. They found that at high speeds, as the modal wave moves upstream, the increase of flow velocity would reduce the modal critical frequency. As a consequence, the acoustics radiation efficiency under the critical frequency of the plate would be higher. Kou et al. [13] also conducted a research for the effect of convection velocity in the TBL on the radiation efficiency. Kou et al. found that the modal averaged radiation efficiency will increase with the increase of the convection velocity below the hydrodynamic coincidence frequency. The study also showed that the increase of the structural loss factor could increase the modal average radiation efficiency at the subcritical frequencies, and the damping effect increases with the increase of the flow velocity.

For a plate subjected to a TBL fluctuation, although a large amount of research work used experimental and computational methods for the vibro-acoustical properties of plates, it is worth a chapter to introduce the prediction model and summarize recent findings for TBL induced plate vibrations and noise radiations. The following sections begins with a description of models for the wavenumber-frequency spectrum of TBL, and then a specific presentation of the calculation of vibro-acoustic responses of the wall plate excited by TBL is followed. In the end, the effect of flow velocity (M_c) and structural damping on the modal averaged radiation efficiency is discussed.

2. Models for the wavenumber-frequency spectrum of turbulent boundary layer fluctuating pressure

As for the research about wavenumber-frequency spectrum of turbulent boundary layer, Corcos [14], Efimtsov [15], Smolyakov-Tkachenko [16], Williams [17], Chase [18, 19] and other researchers put up with a series of widely used of wavenumber-frequency spectrum model. The models are established according to a large number of experimental data and statistical theory of turbulence. The following parts introduce some typical wavenumber-frequency spectrum models.

2.1 The Corcos model

The model proposed by Corcos during the last few decades has been widely used for many different types of problems. The model is applicable in the immediate neighborhood of the so-called convective ridge [20], as long as $\omega\delta/U_\infty > 1$. In this

expression δ is the thickness of the boundary layer and U_∞ the velocity of the flow well away from the structure. The flat-plate boundary layer is taken to lie in the x - y plane of a Cartesian coordinate system, with mean flow in the direction of the x -axis. Corcos assumes that the cross power spectral density, between the pressures at two different positions separated by the vector \mathbf{n} can be expressed as

$$S_{pp}(\xi_x, \xi_y, \omega) = \Phi_{pp}(\omega) \exp(-\gamma_1 k_c |\xi_x|) \exp(-\gamma_3 k_c |\xi_y|) \exp(-jk_c \xi_x) \quad (1)$$

where $\Phi_{pp}(\omega)$ is the auto-power spectral density of turbulent boundary layer fluctuating pressure, $k_c = \omega/U_c$ is the convection wave number. γ_1 and γ_3 can be obtained by fitting experimental data, γ_1 and γ_3 are 0.11–0.12 and 0.7–0.12 respectively for smooth rigid siding.

The Fourier Transform of ξ_x and ξ_y can obtain wavenumber-frequency spectrum

$$\begin{aligned} S_{pp}(k_x, k_y, \omega) &= \iint S_{pp}(\xi_x, \xi_y, \omega) \exp[j(k_x \xi_x + k_y \xi_y)] d\xi_x d\xi_y \\ &= \Phi_{pp}(\omega) \frac{2\gamma_1 k_c}{(k_x - k_c)^2 + (\gamma_1 k_c)^2} \cdot \frac{2\gamma_3 k_c}{k_y^2 + (\gamma_3 k_c)^2} \end{aligned} \quad (2)$$

So, the normalized wavenumber-frequency spectrum in wavenumber domain is

$$\begin{aligned} \hat{S}_{pp}(k_x, k_y, \omega) &= \frac{k_c^2}{\Phi_{pp}(\omega)} S_{pp}(k_x, k_y, \omega) \\ &= \frac{2\gamma_1}{(k_x/k_c - 1)^2 + \gamma_1^2} \cdot \frac{2\gamma_3}{(k_y/k_c)^2 + \gamma_3^2} \end{aligned} \quad (3)$$

2.2 The generalized Corcos model

Caiazzo and Desmet [21] proposed a generalized model which based on the Corcos model. The model uses butterworth filter to replace exponential decay of x and y direction in the Corcos model. It can make the wavenumber-frequency spectrum attenuation rapidly near the convection wave number by adjusting the parameters. Expression of this model is as follows

$$\begin{aligned} S_{pp}(\xi_x, \xi_y, \omega) &= -\Phi_{pp}(\omega) \sin(\pi/2P) \sin(\pi/2Q) \exp(-jk_c \xi_x) \\ &\quad \times \sum_{p=0}^{P-1} \exp[j(\theta_p + \gamma_1 k_c |\xi_x|)] \times \sum_{q=0}^{Q-1} \exp[j(\theta_q + \gamma_3 k_c |\xi_y|)] \end{aligned} \quad (4)$$

where $\theta_p = (\pi/2P) \cdot (1 + 2p)$, $\theta_q = (\pi/2Q) \cdot (1 + 2q)$. When $P = Q = 1$, Eq. (4) is equal to the Corcos model.

Analogously, the normalized wavenumber-frequency spectrum in wavenumber domain is

$$\begin{aligned} \hat{S}_{pp}(k_x, k_y, \omega) &= -\frac{k_c^2}{\pi^2} \frac{PQ(\gamma_1 k_c)^{2P-1}}{\left[(k_x - k_c)^{2P} + (\gamma_1 k_c)^{2P}\right] \sum_{p=0}^{P-1} e^{j\theta_p}} \\ &\quad \times \frac{Q(\gamma_3 k_c)^{2Q-1}}{\left[(k_y)^{2Q} + (\gamma_3 k_c)^{2Q}\right] \sum_{q=0}^{Q-1} e^{j\theta_q}} \end{aligned} \quad (5)$$

2.3 The Efimtsov model

The Efimtsov model assumes, as in the Corcos model, that the lateral and the longitudinal effects of the TBL can be separated. However, in the Efimtsov model the dependence of spatial correlation on boundary layer thickness, δ , as well as spatial separation is taken into account. Correlation length $1/\gamma_1 k_c$ and $1/\gamma_3 k_c$ in Corcos model are replaced with Λ_x and Λ_y . The Efimtsov model gives the cross power spectral density of the pressure at two different positions separated by the vector ξ as

$$S_{pp}(\xi_x, \xi_y, \omega) = \Phi_{pp}(\omega) \exp(-|\xi_x|/\Lambda_x) \exp(-|\xi_y|/\Lambda_y) \exp(-jk_c \xi_x) \quad (6)$$

where

$$\Lambda_x = \delta \left[\left(\frac{a_1 Sh}{U_c/U_\tau} \right)^2 + \frac{a_2^2}{Sh^2 + (a_2/a_3)^2} \right]^{-1/2} \quad (7)$$

$$\Lambda_y = \begin{cases} \delta \left[\left(\frac{a_4 Sh}{U_c/U_\tau} \right)^2 + \frac{a_5^2}{Sh^2 + (a_5/a_6)^2} \right]^{-1/2}, & M_\infty < 0.75 \\ \delta \left[\left(\frac{a_4 Sh}{U_c/U_\tau} \right)^2 + a_7^2 \right]^{-1/2}, & M_\infty > 0.9 \end{cases} \quad (8)$$

where Sh is the Strouhal number and equal to $Sh = \omega\delta/U_\tau$ and U_τ the friction velocity which varies with the Reynolds number but is typically of the order $0.03 U_\infty - 0.04 U_\infty$. At high frequencies these expressions correspond to a Corcos model with $\gamma_1 = 0.1$ and $\gamma_3 = 0.77$. Coefficient a_1 – a_7 are 0.1, 72.8, 1.54, 0.77, 548, 13.5 and 5.66 respectively. When $0.75 < M_\infty < 0.9$, the Λ_y can be determined by numerical interpolation. At high frequency, the Efimtsov model and the Corcos model are equal while $\gamma_1 = 0.10$ and $\gamma_3 = 0.77$.

The normalized wavenumber-frequency spectrum is

$$\hat{S}_{pp}(k_x, k_y, \omega) = \frac{2\Lambda_x^{-1}}{(k_x/k_c - 1)^2 + (\Lambda_x k_c)^{-2}} \cdot \frac{2\Lambda_y^{-1}}{k_y^2 + \Lambda_y^{-2}} \quad (9)$$

2.4 The Smolyakov-Tkachenko model

Like Efimtsov model, Smolyakov-Tkachenko model also takes the boundary layer thickness and scale space separation of boundary layer effect of fluctuating pressure into account. Based on the experimental results, the difference is that the Smolyakov-Tkachenko model amend the space scale function index

$\exp[-(|\xi_x|/\Lambda_x + |\xi_y|/\Lambda_y)]$ to $\exp\left[-\sqrt{(\xi_x^2/\Lambda_x^2 + \xi_y^2/\Lambda_y^2)}\right]$, in order to make the computing result is consistent with the experimental results.

The normalized wavenumber-frequency spectrum is

$$\hat{S}_{pp}(k_x, k_y, \omega) = 0.974A(\omega)h(\omega)[F(k_x, k_y, \omega) - \Delta F(k_x, k_y, \omega)] \quad (10)$$

where

$$A(\omega) = 0.124 \left[1 - \frac{1}{4k_c \delta^*} + \left(\frac{1}{4k_c \delta^*} \right)^2 \right]^{1/2} \quad (11)$$

$$h(\omega) = \left[1 - \frac{m_1 A}{6.515 \sqrt{G}} \right]^{-1} \quad (12)$$

$$m_1 = \frac{1 + A^2}{1.025 + A^2} \quad (13)$$

$$G = 1 + A^2 - 1.005 m_1 \quad (14)$$

$$F(k_x, k_y, \omega) = \left[A^2 + (1 - k_x/k_c)^2 + \left(\frac{k_y/k_c}{6.45} \right)^2 \right]^{-3/2} \quad (15)$$

$$\Delta F(k_x, k_y, \omega) = 0.995 \left[1 + A^2 + \frac{1.005}{m_1} \left\{ (m_1 - k_x/k_c)^2 + (k_y/k_c)^2 - m_1^2 \right\} \right]^{-3/2} \quad (16)$$

where δ^* is the thickness of boundary layer, which is also set as $\delta^* = \delta/8$.

2.5 The Ffowcs-Williams model

Ffowcs-Williams using Lighthill acoustic analogy theory to deduce a frequency-wave spectrum model, in which the speed of the pneumatic equation is set as the source term by Corcos form. A number of parameters in the model and function need further experiments to determine, which is not widely used at present. Hwang and Geib [22] ignore compression factor of the influence of this model to put forward a simplified model. The normalized wavenumber-frequency spectrum is

$$\hat{S}_{pp}(k_x, k_y, \omega) = \left(\frac{|k|}{k_c} \right)^2 \frac{2\gamma_1}{(k_x/k_c - 1)^2 + \gamma_1^2} \cdot \frac{2\gamma_3}{(k_y/k_c)^2 + \gamma_3^2} \quad (17)$$

2.6 The Chase model

Chase's model is another model commonly used and believed to describe the low-wavenumber domain better than Corcos's model, which has the same starting point with the Ffowcs-Williams model. The normalized wavenumber-frequency spectrum can be described as

$$\hat{S}_{pp}(k_x, k_y, \omega) = \frac{(2\pi)^3 \rho k_c^2 U_\tau^3}{\Phi(\omega)} \left(C_M k_x^2 K_M^{-5} + C_T |k|^2 K_T^{-5} \right) \quad (18)$$

where

$$K_M^2 = \frac{(\omega - U_c k_x)^2}{h^2 U_\tau^2} + |k|^2 + (b_M \delta)^{-2} \quad (19)$$

$$K_T^2 = \frac{(\omega - U_c k_x)^2}{h^2 U_\tau^2} + |k|^2 + (b_T \delta)^{-2} \quad (20)$$

$$\Phi(\omega) = \frac{(2\pi)^2 \rho^2 h U_\tau^4}{3\omega(1 + \mu^2)} (C_M F_M + C_T F_T) \quad (21)$$

$$F_M = [1 + \mu^2 \alpha_M^2 + \mu^4 (\alpha_M^2 - 1)] / [\alpha_M^2 + \mu^2 (\alpha_M^2 - 1)]^{3/2} \quad (22)$$

$$F_T = [1 + \alpha_T^2 + \mu^2 (3\alpha_T^2 - 1) + 2\mu^4 (\alpha_T^2 - 1)] / [\alpha_T^2 + \mu^2 (\alpha_T^2 - 1)]^{3/2} \quad (23)$$

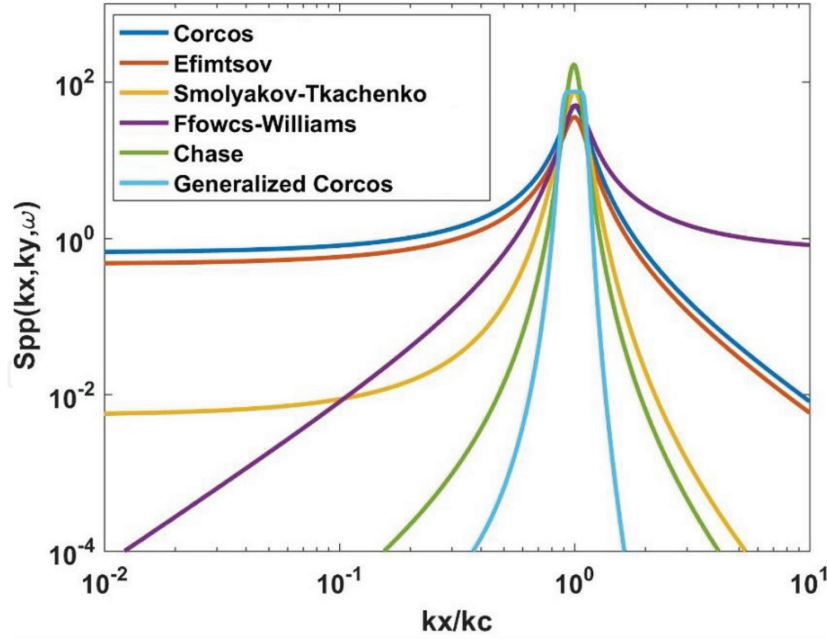


Figure 1.

A comparison of models for different wavenumber-frequency spectrum of turbulent boundary layer fluctuating pressure, reproduced from Ref. [23].

$$\alpha_M^2 = 1 + (b_M k_c \delta)^{-2}, \quad \alpha_T^2 = 1 + (b_T k_c \delta)^{-2} \quad (24)$$

$$\mu = h U_\tau / U_c \quad (25)$$

$$C_M = 0.0745, C_T = 0.0475, b_M = 0.756, b_T = 0.378, h = 3.0 \quad (26)$$

2.7 Comparison of models

Figure 1 shows the comparison of the above models. In the figure, the parameters used by the Corcos model are $\gamma_1 = 0.116$, $\gamma_3 = 0.77$, the order of Generalized Corcos model is ($P = 1$, $Q = 4$). From the comparison among those models, it can be seen that the Generalized Corcos model attenuates quickly in the vicinity of the convective wave number, and its order is adjustable, which can effectively control the computational accuracy. The model can obtain more accurate prediction results by adjusting parameters. In addition, the Chase model is considered to be able to better describe the pressure characteristics of TBL pulsation at low wave number segment, while other models have some defects at low wave number segment. However, Corcos model is the most commonly used in practical application. Because the model is simple in form and has clear physical significance, a simple calculation formula can usually be obtained when solving the structural vibration and sound response induced by turbulent boundary layer. It should be noted that the structure radiated sound predicted by Corcos model tends to be larger at low wave number.

3. Calculation of vibro-acoustic responses of the wall plate excited by TBL

Consider a simply supported thin rectangular plate excited by TBL, as shown in **Figure 2**. In the figure, U_c is turbulent flow velocity, and the direction of the incoming flow is parallel to the X-axis. In this chapter, vibro-acoustic responses are solved by modal superposition method [23].

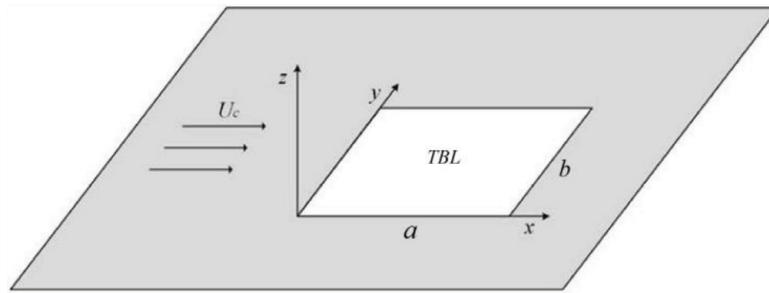


Figure 2.
Schematic diagram of simply supported thin rectangular plate excited by TBL.

Assume that point s on the plate is excited by a normal force F at points, and the vibration displacement response at point r can be calculated by

$$W(\mathbf{r}, \omega) = H(\mathbf{r}, \mathbf{s}, \omega) \cdot F(\mathbf{s}, \omega) \quad (27)$$

where $\mathbf{s} = (x_0, y_0)$, $\mathbf{r} = (x, y)$.

The impulse response H satisfies the following governing equation

$$[D(1 + j\eta)\nabla^4 - m_s\omega^2]H(\mathbf{r}, \mathbf{s}, \omega) = \delta(\mathbf{r} - \mathbf{s}) \quad (28)$$

The impulse response can be expanded as

$$H(\mathbf{r}, \mathbf{s}, \omega) = \sum_{m=1}^M \sum_{n=1}^N H_{mn}(\omega) \Psi_{mn}(\mathbf{r}) \Psi_{mn}(\mathbf{s}) \quad (29)$$

The modal amplitude of impulse response by using the Galerkin method can be described as

$$H_{mn}(\omega) = \frac{1}{DK_{mn}(1 + j\eta) - m_s\omega^2} \quad (30)$$

3.1 Vibro-acoustic responses of plate solved by spatial domain integration

Cross spectral density of displacement response for any two points on the plate can be defined as

$$\begin{aligned} S_{WW}(\mathbf{r}_1, \mathbf{r}_2, \omega) &= \int_S \int_S S_{pp}(\mathbf{s}_1 - \mathbf{s}_2, \omega) H^*(\mathbf{r}_1, \mathbf{s}_1, \omega) H(\mathbf{r}_2, \mathbf{s}_2, \omega) d\mathbf{s}_1 d\mathbf{s}_2 \\ &= \Phi_{pp}(\omega) \sum_{m=1}^M \sum_{n=1}^N |H_{mn}(\omega)|^2 \Psi_{mn}(\mathbf{r}_1) \Psi_{mn}(\mathbf{r}_2) J_{mn}(\omega) \end{aligned} \quad (31)$$

where

$$J_{mn}(\omega) = \int_S \int_S S_{pp}(\mathbf{s}_1 - \mathbf{s}_2) \Psi_{mn}(\mathbf{s}_1) \Psi_{mn}(\mathbf{s}_2) d\mathbf{s}_1 d\mathbf{s}_2 \quad (32)$$

In the above equation, $J_{mn}(\omega)$ is called modal excitation term.

When using the Corcos model, the coordinate transformation of the quadruple integral in the modal excitation term can be obtained

$$J_{mn}(\omega) = \frac{4}{S} \left(\frac{1}{k_m k_n} J_{mn}^1 + J_{mn}^2 + \frac{1}{k_m} J_{mn}^3 + \frac{1}{k_n} J_{mn}^4 \right) \quad (33)$$

Where

$$\begin{Bmatrix} J_{mn}^1 \\ J_{mn}^2 \\ J_{mn}^3 \\ J_{mn}^4 \end{Bmatrix} = \int_0^b \int_0^a \begin{Bmatrix} 1 \\ (a-x)(b-y) \\ (b-y) \\ (a-x) \end{Bmatrix} \times \begin{Bmatrix} \sin k_m x \cdot \sin k_n y \\ \cos k_m x \cdot \cos k_n y \\ \sin k_m x \cdot \cos k_n y \\ \cos k_m x \cdot \sin k_n y \end{Bmatrix} \tilde{S}_{pp}(x, y, \omega) dx dy \quad (34)$$

$$\tilde{S}_{pp}(x, y, \omega) = \exp(-\gamma_1 k_c x) \exp(-\gamma_3 k_c y) \cos(k_c x) \quad (35)$$

When $r_1 = r_2$, the auto-spectral density of displacement response can be obtained as

$$S_{WW}(\mathbf{r}, \omega) = \Phi_{pp}(\omega) \sum_{m=1}^M \sum_{n=1}^N |H_{mn}(\omega)|^2 \Psi_{mn}^2(\mathbf{r}) J_{mn}(\omega) \quad (36)$$

As for vibration ($V = j\omega W$) the auto-spectral density is

$$\begin{aligned} S_{VV}(\mathbf{r}, \omega) &= \omega^2 S_{WW}(\mathbf{r}, \omega) \\ &= \omega^2 \Phi_{pp}(\omega) \sum_{m=1}^M \sum_{n=1}^N |H_{mn}(\omega)|^2 \Psi_{mn}^2(\mathbf{r}) J_{mn}(\omega) \end{aligned} \quad (37)$$

So, vibration energy and acoustic radiation energy can be expressed as

$$\begin{aligned} \langle V^2 \rangle &= \frac{1}{S} \iint S_{VV}(x, y, \omega) dS \\ &= \frac{1}{S} \omega^2 \Phi_{pp}(\omega) \sum_{m=1}^M \sum_{n=1}^N J_{mn}(\omega) |H_{mn}(\omega)|^2 \end{aligned} \quad (38)$$

$$\Pi^r = \rho_0 c_0 \omega^2 \Phi_{pp}(\omega) \sum_{m=1}^M \sum_{n=1}^N \sigma_{mn} J_{mn}(\omega) |H_{mn}(\omega)|^2 \quad (39)$$

According to the definition, the modal average acoustic radiation efficiency excited by TBL of the thin plate is

$$\sigma = \frac{\sum_{m=1}^M \sum_{n=1}^N \sigma_{mn} J_{mn}(\omega) |H_{mn}(\omega)|^2}{\sum_{m=1}^M \sum_{n=1}^N J_{mn}(\omega) |H_{mn}(\omega)|^2} \quad (40)$$

3.2 Vibro-acoustic responses of plate solved by wavenumber domain integration

Another approach to obtain the cross spectral density of vibration response is to solve it directly by using the separable integral property of some turbulent boundary layer pulsating pressure models in the wavenumber domain [24].

The wavenumber-frequency spectrum of TBL satisfies the following relationship

$$\begin{aligned} S_{pp}(\mathbf{s}_1 - \mathbf{s}_2, \omega) &= \frac{1}{(2\pi)^2} \int S_{pp}(\mathbf{k}, \omega) \exp[-j\mathbf{k}(\mathbf{s}_1 - \mathbf{s}_2)] d\mathbf{k} \\ &= \frac{1}{(2\pi)^2} \int \int S_{pp}(k_x, k_y, \omega) \exp[-j(k_x \xi_x + k_y \xi_y)] dk_x dk_y \end{aligned} \quad (41)$$

where $\mathbf{s}_1 - \mathbf{s}_2 = (\xi_x, \xi_y)$, $\mathbf{k} = (k_x, k_y)$.

The formula can be obtained by substituting the cross spectral density of the vibration response

$$\begin{aligned}
 S_{WW}(\mathbf{r}_1, \mathbf{r}_2, \omega) &= \iint S_{pp}(\mathbf{s}_1, \mathbf{s}_2, \omega) H^*(\mathbf{r}_1, \mathbf{s}_1, \omega) H(\mathbf{r}_2, \mathbf{s}_2, \omega) d\mathbf{s}_1 d\mathbf{s}_2 \\
 &= \frac{1}{(2\pi)^2} \int S_{pp}(\mathbf{k}, \omega) \exp[-j\mathbf{k}(\mathbf{s}_1 - \mathbf{s}_2)] d\mathbf{k} \iint H^*(\mathbf{r}_1, \mathbf{s}_1, \omega) H(\mathbf{r}_2, \mathbf{s}_2, \omega) d\mathbf{s}_1 d\mathbf{s}_2 \\
 &= \frac{1}{(2\pi)^2} \int S_{pp}(\mathbf{k}, \omega) d\mathbf{k} \int H^*(\mathbf{r}_1, \mathbf{s}_1, \omega) \exp(-j\mathbf{k}\mathbf{s}_1) d\mathbf{s}_1 \int H(\mathbf{r}_2, \mathbf{s}_2, \omega) \exp(j\mathbf{k}\mathbf{s}_2) d\mathbf{s}_2 \\
 &= \frac{1}{(2\pi)^2} \int S_{pp}(\mathbf{k}, \omega) G^*(\mathbf{r}_1, \mathbf{k}, \omega) G(\mathbf{r}_2, \mathbf{k}, \omega) d\mathbf{k}
 \end{aligned} \tag{42}$$

where

$$\begin{aligned}
 G(\mathbf{r}, \mathbf{k}, \omega) &= \int H(\mathbf{r}, \mathbf{s}, \omega) \exp(j\mathbf{k}\mathbf{s}) d\mathbf{s} \\
 &= \sum_{m=1}^M \sum_{n=1}^N H_{mn}(\omega) \Psi_{mn}(\mathbf{r}) \int \Psi_{mn}(\mathbf{s}) \exp(j\mathbf{k}\mathbf{s}) d\mathbf{s} \\
 &= \sum_{m=1}^M \sum_{n=1}^N H_{mn}(\omega) \Psi_{mn}(\mathbf{r}) I_{mn}(\mathbf{k})
 \end{aligned} \tag{43}$$

$$\begin{aligned}
 I_{mn}(\mathbf{k}) &= \int \Psi_{mn}(\mathbf{s}) \exp(j\mathbf{k}\mathbf{s}) d\mathbf{s} \\
 &= \frac{2}{\sqrt{ab}} \int_0^b \int_0^a \sin(k_m x) \sin(k_n y) \exp[j(k_x x + k_y y)] dx dy \\
 &= \frac{2}{\sqrt{ab}} \cdot \frac{k_m [1 - \cos(m\pi) \exp(jk_x a)]}{k_x^2 - k_m^2} \cdot \frac{k_n [1 - \cos(n\pi) \exp(jk_y b)]}{k_y^2 - k_n^2}
 \end{aligned} \tag{44}$$

Similarly, the spectral density of the vibration velocity can be obtained as

$$\begin{aligned}
 S_{VV}(\mathbf{r}, \omega) &= \frac{\omega^2}{(2\pi)^2} \int S_{pp}(\mathbf{k}, \omega) |G(\mathbf{r}, \mathbf{k}, \omega)|^2 d\mathbf{k} \\
 &= \frac{\omega^2}{(2\pi)^2} \sum_{m=1}^M \sum_{n=1}^N \Psi_{mn}^2(\mathbf{r}) |H_{mn}(\omega)|^2 \int S_{pp}(\mathbf{k}, \omega) |I_{mn}(\mathbf{k})|^2 d\mathbf{k}
 \end{aligned} \tag{45}$$

As for the Corcos model, we can obtain that

$$\int S_{pp}(\mathbf{k}, \omega) |I_{mn}(\mathbf{k})|^2 d\mathbf{k} = \frac{4}{S} \Phi_{pp}(\omega) [2\gamma_1 k_c \Lambda_m(\omega)] [2\gamma_3 k_c \Gamma_n(\omega)] \tag{46}$$

where

$$\Lambda_m(\omega) = 2k_m^2 \int_{-\infty}^{\infty} \frac{1 - \cos(m\pi) \cos(k_x a)}{(k_x^2 - k_m^2)^2 [(k_x - k_c)^2 + (\gamma_1 k_c)^2]} dk_x \tag{47}$$

$$\Gamma_n(\omega) = 2k_n^2 \int_{-\infty}^{\infty} \frac{1 - \cos(n\pi) \cos(k_y b)}{(k_y^2 - k_n^2)^2 [k_y^2 + (\gamma_3 k_c)^2]} dk_y \quad (48)$$

According to the residue theorem, $\Lambda_m(\omega)$ and $\Gamma_n(\omega)$ can be further simplified as

$$\begin{aligned} \Lambda_m(\omega) &= 2k_m^2 \int_{-\infty}^{\infty} \frac{1 - \cos(m\pi) \cos(k_x a)}{(k_x^2 - k_m^2)^2 [(k_x - k_c)^2 + (\gamma_1 k_c)^2]} dk_x \\ &= 2\pi k_m^2 \left\{ \frac{a}{4k_m^2 [(k_m + k_c)^2 + (\gamma_1 k_c)^2]} + \frac{a}{4k_m^2 [(k_m - k_c)^2 + (\gamma_1 k_c)^2]} \right. \end{aligned} \quad (49)$$

$$\begin{aligned} &+ \frac{1 - \cos(m\pi) \exp[-(j + \gamma_1)k_c a]}{(2\gamma_1 k_c) [k_c^2 (1 - j\gamma_1)^2 - k_m^2]^2} + \frac{1 - \cos(m\pi) \exp[(j - \gamma_1)k_c a]}{(2\gamma_1 k_c) [k_c^2 (1 + j\gamma_1)^2 - k_m^2]^2} \Bigg\} \\ \Gamma_n(\omega) &= 2k_n^2 \int_{-\infty}^{\infty} \frac{1 - \cos(n\pi) \cos(k_y b)}{(k_y^2 - k_n^2)^2 [k_y^2 + (\gamma_3 k_c)^2]} dk_y \\ &= 2\pi k_n^2 \left\{ \frac{b}{2k_n^2 [k_n^2 + (\gamma_3 k_c)^2]} + \frac{1 - \cos(n\pi) \exp(-\gamma_3 k_c b)}{(\gamma_3 k_c) [k_n^2 + (\gamma_3 k_c)^2]^2} \right\} \end{aligned} \quad (50)$$

Vibration energy and sound radiation energy are

$$\begin{aligned} \langle V^2 \rangle &= \frac{\omega^2}{(2\pi)^2 S} \int \int S_{pp}(\mathbf{k}, \omega) |G(\mathbf{r}, \mathbf{k}, \omega)|^2 d\mathbf{k} d\mathbf{r} \\ &= \frac{\omega^2}{(2\pi)^2 S} \sum_{m=1}^M \sum_{n=1}^N |H_{mn}(\omega)|^2 \int S_{pp}(\mathbf{k}, \omega) |I_{mn}(\mathbf{k})|^2 d\mathbf{k} \end{aligned} \quad (51)$$

$$\begin{aligned} &= \frac{1}{S} \omega^2 \Phi_{pp}(\omega) \left(\frac{4\gamma_1 k_c \gamma_3 k_c}{S \pi} \right) \sum_{m=1}^M \sum_{n=1}^N \Lambda_m(\omega) \Gamma_n(\omega) |H_{mn}(\omega)|^2 \\ \Pi^r &= \frac{1}{(2\pi)^2} \rho_0 c_0 \omega^2 \sum_{m=1}^M \sum_{n=1}^N \sigma_{mn} |H_{mn}(\omega)|^2 \int S_{pp}(\mathbf{k}, \omega) |I_{mn}(\mathbf{k})|^2 d\mathbf{k} \\ &= \rho_0 c_0 \omega^2 \Phi_{pp}(\omega) \left(\frac{4\gamma_1 k_c \gamma_3 k_c}{S \pi} \right) \sum_{m=1}^M \sum_{n=1}^N \sigma_{mn} \Lambda_m(\omega) \Gamma_n(\omega) |H_{mn}(\omega)|^2 \end{aligned} \quad (52)$$

Compare the above two equations, it can be seen that

$$J_{mn}(\omega) = \frac{4}{S} \left[\frac{\gamma_1 k_c}{\pi} \Lambda_m(\omega) \right] \times \left[\frac{\gamma_3 k_c}{\pi} \Gamma_n(\omega) \right] \quad (53)$$

Finally, the modal average acoustic radiation efficiency can be obtained as

$$\sigma = \frac{\sum_{m=1}^M \sum_{n=1}^N \sigma_{mn} \Lambda_m(\omega) \Gamma_n(\omega) |H_{mn}(\omega)|^2}{\sum_{m=1}^M \sum_{n=1}^N \Lambda_m(\omega) \Gamma_n(\omega) |H_{mn}(\omega)|^2} \quad (54)$$

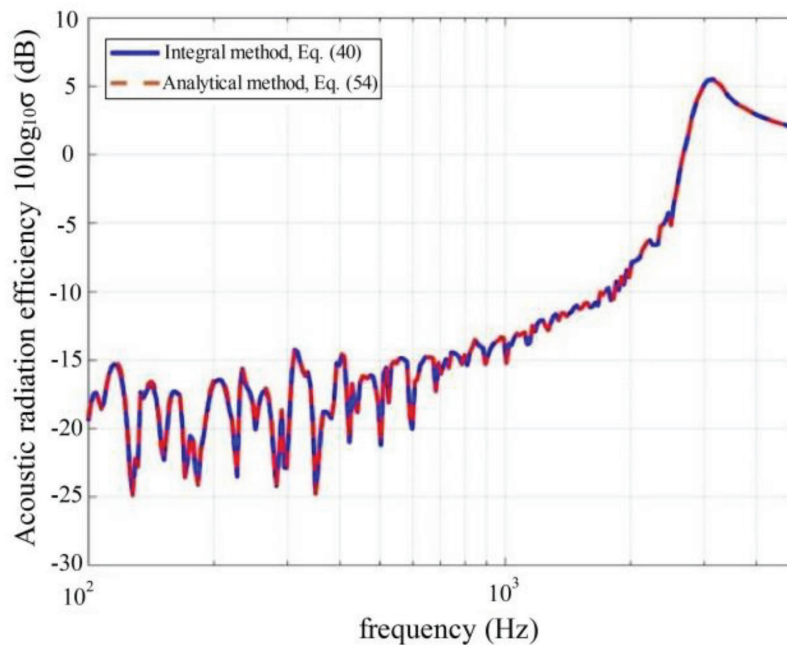


Figure 3.
 Comparison of calculation methods of the modal averaged radiation efficiency excited by TBL. Reproduced from Ref. [23].

By observing the above equation, it can be found that only the modal excitation term in the modal averaged radiation efficiency is related to turbulence.

Figure 3 shows the comparison of two methods for calculating the modal averaged radiation efficiency excited by TBL. The size of the plate is 1.25×1.1 m, and the thickness is 4 mm, structural loss factor of aluminum plate is 1%, mach number is 0.5. Obviously, the accuracy of the two methods is equal. Computation speed of analytical method is much faster than integral method, but its range of application has limitations. Only the Corcos model and Efimtsov model can be used to separate integrals in the wave number domain.

The comparison of measured and predicted velocity spectral density and the radiated sound intensity of a plate ($a \times b = 0.62 \times 0.3$ m, and the thickness is 1.1 mm) is shown in **Figure 4**, which is only compared in narrow band. In this study, the loss factor of the plate assumes as 1.5%. The measured and predicted results for radiated sound intensity and auto spectrum of velocity have a good agreement with the frequency ranges from 100 to 3500 Hz. The agreement of the two type curves provides solid verification to test measured and predicted results.

3.3 Characteristic frequency in hydrodynamic coincidence

When the velocity of bending wave in the wall plate is close to the sound velocity in the air, the sound radiation efficiency reaches the maximum value. The corresponding frequency is the so-called critical frequency, and its expression is

$$f_c = \frac{c_0^2}{2\pi} \sqrt{\frac{m_s}{D}} \quad (55)$$

In the case of flow, when the velocity of flexural wave propagation in the wall plate is close to the turbulent convection velocity, the wall plate is most excited by the fluctuating pressure of TBL. The corresponding frequency is defined as the hydrodynamic coincidence frequency

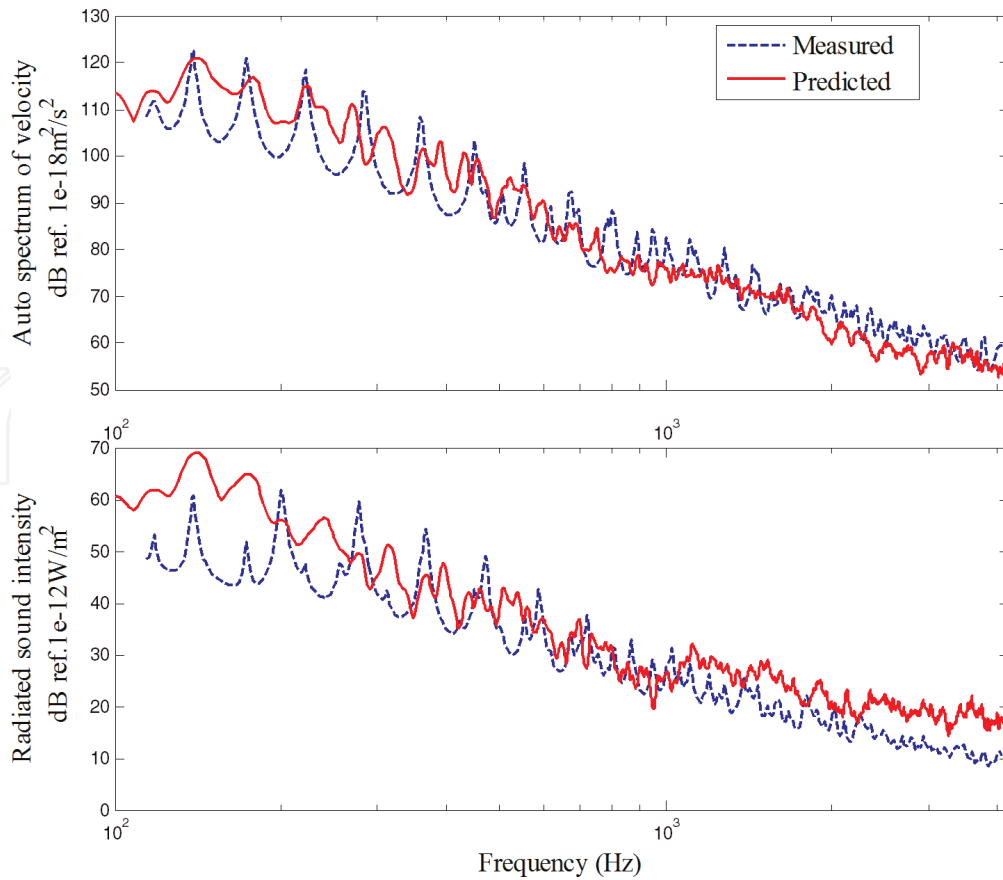


Figure 4. Measured and predicted velocity auto spectrum and the radiated sound intensity of the plate with the size of $a \times b = 0.62 \times 0.3$ m. Narrow band analysis in per Hz. Flow speed 86 m/s.

$$f_h = \frac{U_c^2}{2\pi} \sqrt{\frac{m_s}{D}} \quad (56)$$

Similarly, for order (m, n) mode, its critical frequency and hydrodynamic coincidence frequency are

$$f_{c,mn} = \frac{c_0}{2\pi} k_{mn} \quad (57)$$

$$f_{h,mn} = \frac{U_c}{2\pi} k_{mn} \quad (58)$$

In conclusion, the relationship between critical frequency and hydrodynamic coincidence frequency can be summarized as follows

$$f_h = M_c^2 \cdot f_c \quad (59)$$

$$f_{h,mn} = M_c \cdot f_{c,mn} \quad (60)$$

In the above two equations, $M_c = U_c/c_0$ is mach number. Subsonic turbulence is generally considered, so the hydrodynamic coincidence frequency is always less than the critical frequency of the plate. It is important to note that the characteristics of frequency is a reference value which is based on the infinite plate hypothesis. Actually, the characteristics frequency of the limited plate slightly higher than a reference value. In addition, for the transverse flow problem, modal power line frequency can be thought of only related to the transverse mode. That is to say, $f_{h,mn} \approx U_c k_m / 2\pi$, where $k_m = m\pi/a$ is lateral modal wave number.

4. Effect of flow velocity and structural damping on the acoustic radiation efficiency

4.1 Effect of convection velocity on the modal averaged radiation efficiency

The specific parameters and dimensions used in the calculation are listed in Table 1.

The increment of vibration power and acoustic radiation energy are different with the increase of the velocity, which indicates that the changing of velocity can affect the modal averaged radiation efficiency. The modal averaged radiation efficiency of the aluminum plate at three flow velocities ($M_c = 0.5; 0.7; 0.9$) is shown in Figure 5. It can be seen that when the M_c increases from 0.5 to 0.9, the modal averaged radiation efficiency will increase by 3–7 dB below the hydrodynamic coincidence frequency. And the corresponding hydrodynamic coincidence frequencies (f_h) are 1482, 2905, and 4802 Hz, respectively. The results show that the modal averaged radiation efficiency increases in the frequency range below the hydrodynamic coincidence frequency. The increase of the modal averaged radiation efficiency indicates that with the increase of flow velocity, the increment of the radiated sound power is larger than that of the mean square velocity.

The phenomenon that the modal averaged radiation efficiency increases with the flow velocity can be explained by the hydrodynamic coincidence effect. For the lateral incoming flow problem, the hydrodynamic coincidence is mainly

Plate length	a	1.25 m
Plate width	b	1.1 m
Plate thickness	h	0.002 m
Plate surface density	m_s	5.4 kg/m ²
Plate bending stiffness	D	52 Nm
Air density	ρ_0	1.21 kg/m ³
Sound speed	c_0	340 m/s

Table 1.
Parameters used in calculation.

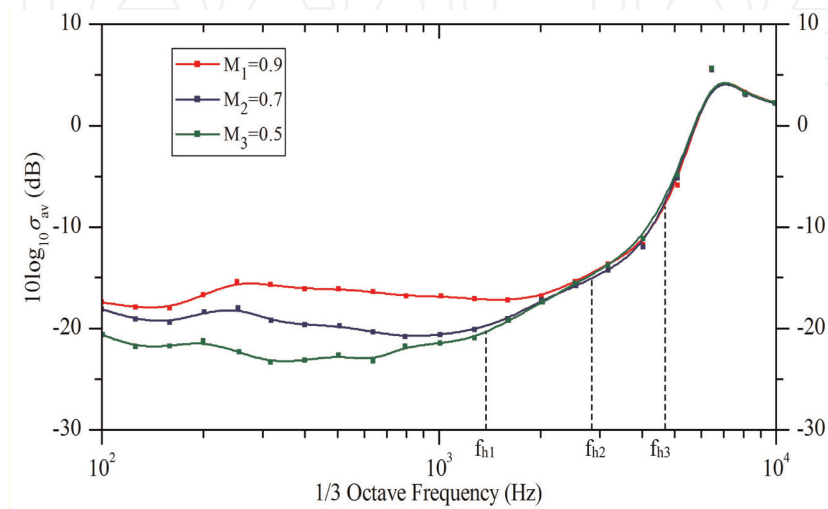


Figure 5.
Effect of the convective Mach number on the modal averaged radiation efficiency of the finite aluminum plate.
Reproduced from Ref. [23].

determined by the lateral modal trace speed and the convection velocity. When the bending wave velocity of the lateral mode is the same as the turbulent flow velocity ($U_c = 2\pi f/k_m$), the corresponding hydrodynamic coincidence frequency is $f = mU_c/2a$. Thus a higher convection velocity at the same frequency will lead the TBL excitation to coincide with a lower order lateral mode.

The reason for above phenomenon may be further explored through the modal excitation terms. As illustrated in **Figure 6**, the lateral modal excitation term ($10\log_{10}\Lambda_m(\omega)$) is plotted with the lateral mode number (m) and frequency for different flow velocity (M_c). In the figure, the peak of the lateral modal excitation term corresponds to the maximum excitation and its position depends on the hydrodynamic coincidence frequency. The black bold lines in the two sub graphs are the positions where the hydrodynamic coincidence occurs. It can be seen that the slope of the hydrodynamic coincidence line is inversely proportional to the flow velocity, and the higher the velocity is, the lower the order of a certain frequency is. In addition, the lateral modes near the hydrodynamic coincidence line are all strongly excited. As the frequency increases, the number of these modes increases, but the amplitude of their corresponding mode excitation term decreases. Below the

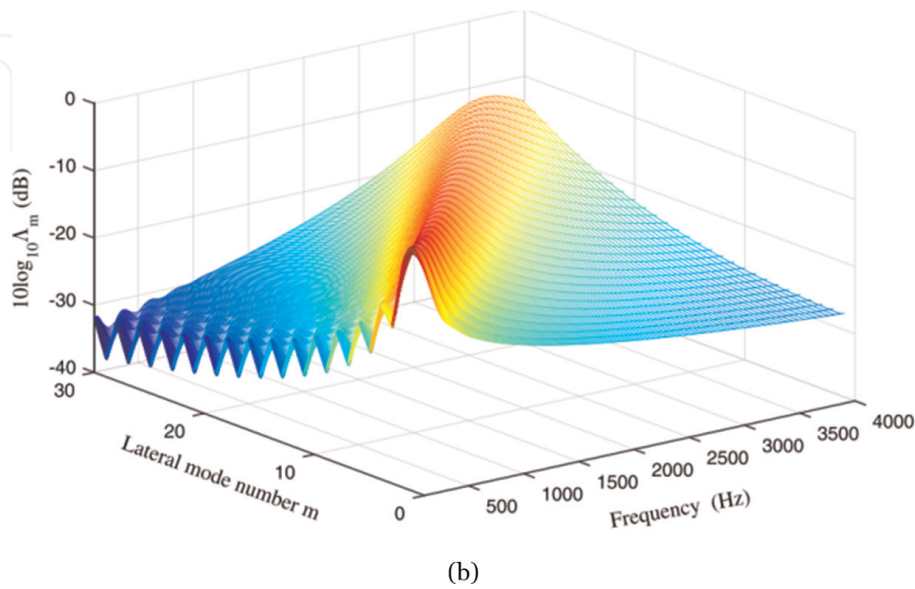
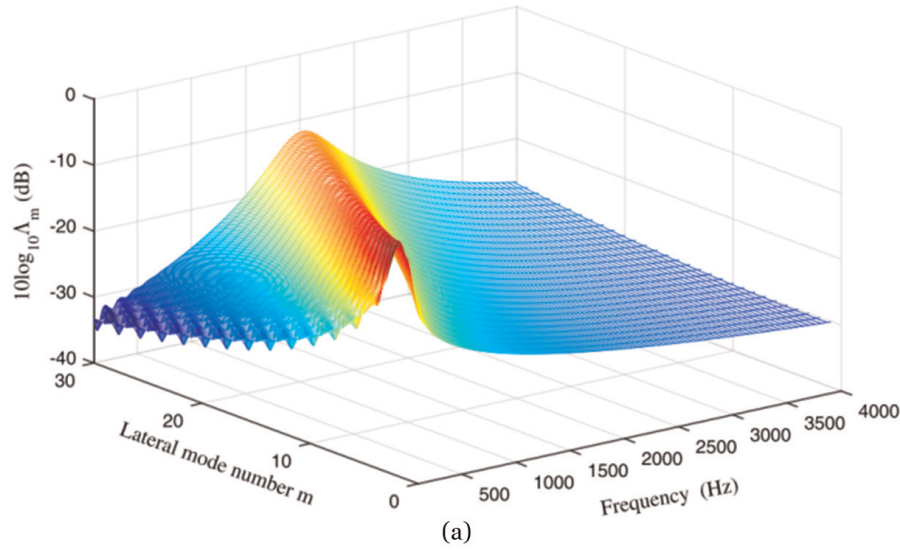


Figure 6. Variation of the lateral modal excitation term with the lateral mode number and the frequency of a finite aluminum plate. (a) Convective $M_c = 0.5$ and (b) convective $M_c = 0.9$. Reproduced from Ref. [13].

critical frequency, a lower order lateral mode always has higher modal averaged radiation efficiency than that of a higher order lateral mode with the same n , since the modal critical frequency moves to lower frequency. So plate with higher flow velocity is supposed to have higher modal averaged radiation efficiency.

As an example, the hydrodynamic coincidence lines for different flow velocity (M_c) and the modal radiation efficiencies of mode $(m, 1)$ are illustrated in **Figure 7**. The black solid lines in the figure are the hydrodynamic coincidence line corresponding to the mode order and frequency. It can be seen that at a certain frequency, the modal averaged radiation efficiency of the hydrodynamic coincidence modes at higher velocity is always greater than that of the low velocity. In a word, an increase of the flow velocity will increase the modal radiation efficiency of the coincided mode, and then results in the increase of the modal averaged radiation efficiency. Besides, owing to the low pass property of the modal excitation term, the increase of the modal radiation efficiency is restrained above the hydrodynamic coincidence frequency. As a consequence, the modal averaged radiation efficiency is great affected by the flow velocity which only occurs below the hydrodynamic coincidence frequency.

4.2 Effect of structural damping on modal averaged radiation efficiency

The modal averaged radiation efficiency changes with structural loss factors for different flow velocity (M_c), as shown in **Figure 8**. The reference value is calculated according to Leppington’s formula [25]. Though Leppington’s formula is widely used in statistical energy analysis, it does not take the flow and structural damping into account. **Figure 8** indicates that an increase of the structural loss factor will increase the modal averaged radiation efficiency under the critical frequency, but the increments are different for different flow velocity. It is found that the modal averaged radiation efficiency is not sensitive to the change of structure loss factor at low Mach number. For example, for a typical high-speed train ($M_c = 0.25$), the increased modal averaged radiation efficiency is less than 2 dB in the frequency band below the critical frequency when the structural loss factor increases from 1 to 4%. In the case of high flow velocity, the effect of structure loss factor on the modal averaged radiation efficiency is much obvious. When $M_c = 0.7$, the modal averaged radiation efficiency will increase by about 5 dB if the structural loss factor has the same increment. The results show that the influence of structural damping on the

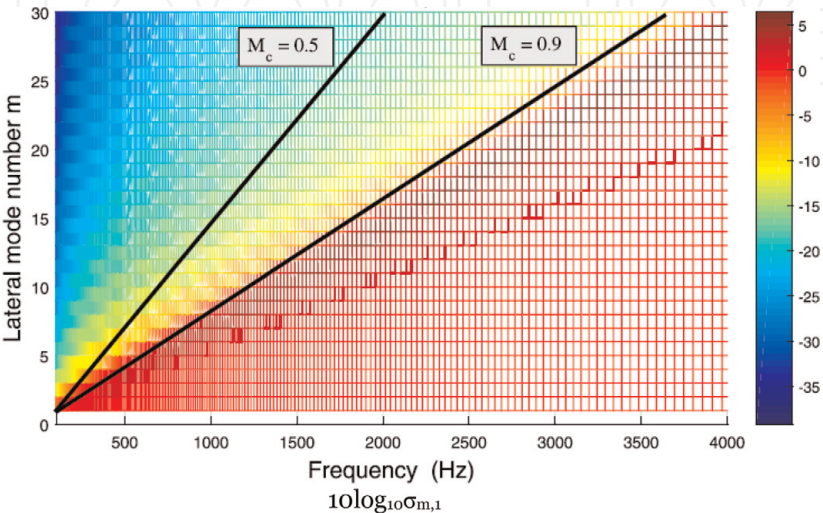
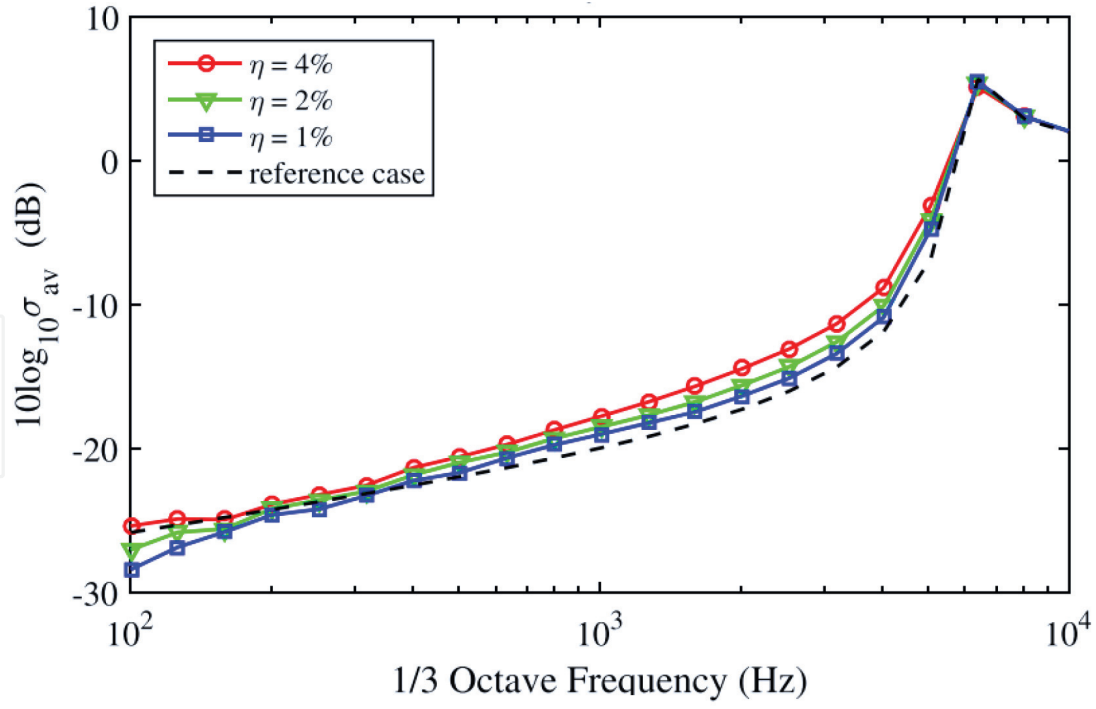
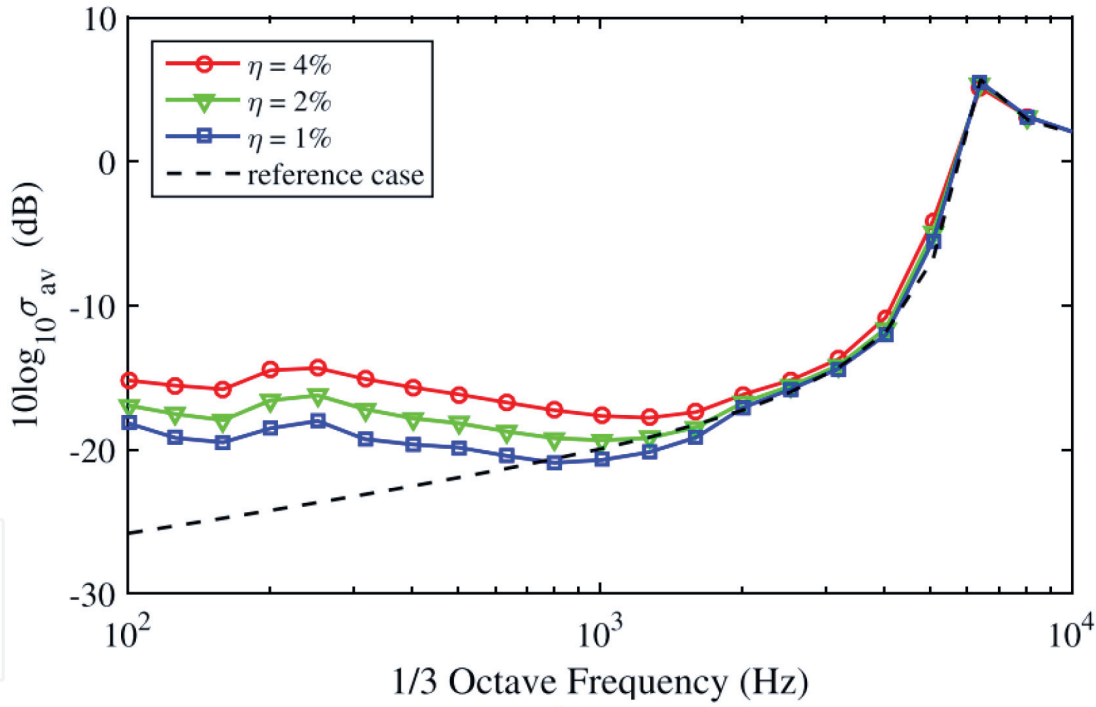


Figure 7. Hydrodynamic coincidence lines and variation of the modal radiation efficiency with the lateral mode number and the frequency of a finite aluminum plate. m varies, $n = 1$. Reproduced from Ref. [13].



(a)



(b)

Figure 8.

Effect of the structural loss factor on the modal averaged radiation efficiency of a finite aluminum plate. (a) Convective $M_c = 0.25$ and (b) convective $M_c = 0.7$. Reproduced from Ref. [13].

modal averaged radiation efficiency is related to the flow velocity, and the influence of structural damping can be enhanced by increasing the flow velocity.

The effect of structural damping on the modal averaged radiation efficiency can be qualitatively explained by Eq. (61)

$$\sigma_{av} = \frac{\Pi^t}{\rho_0 c_0 S \langle V^2 \rangle} = \frac{\sum_{m=1}^{\infty} \sum_{n=1}^{\infty} \sigma_{mn}(\omega) J_{mn}(\omega) |V_{mn}(\omega)|^2}{\sum_{m=1}^{\infty} \sum_{n=1}^{\infty} J_{mn}(\omega) |V_{mn}(\omega)|^2} \quad (61)$$

Eq. (61) shows that the modal averaged radiation efficiency is equivalent to the weighted average function of the modal velocity response, and the weighted coefficient is the modal averaged radiation efficiency. In the frequency band below the critical frequency, the radiation efficiency of each mode varies in the range from 0 to 1. Due to this weighted effect of Eq. (61), the vibration energy (denominator in the equation) decreases more effectively than the acoustic radiation power (molecule in the equation). Thus the radiation efficiency increases in the frequency band below the critical frequency. However, the phenomenon that the radiation efficiency of a damped plate is enlarged with increment of flow velocity has not yet been clearly interpreted.

Moreover, it is observed that the effect of structural damping on modal averaged radiation efficiency has a good agreement with the research of Kou [23] at low flow velocity. In their work, it is shown that the modal averaged radiation efficiency of heavily damped structures is sensitive to the change of structural loss factor without turbulent flow. It also implies that Leppington's equation is not applicable to the prediction of modal averaged radiation efficiency of damped structures at high flow velocity.

5. Conclusion

This chapter studies the vibro-acoustic characteristics of the wall plate structure excited by turbulent boundary layer (TBL). Based on the modal expansion and Corcos model, the formulas for calculating the modal averaged radiation efficiency are derived. The results indicate that an increment of flow rate will increase the vibration energy and the radiated sound energy of the structure. However, the amplitude of two cases varies with the velocity are not the same, and when the velocity increases, the acoustic radiation efficiency will increase below the hydrodynamic coincidence frequency range. The main reason for this phenomenon is that a higher convection velocity will coincide with lower order modes which have higher radiation efficiencies.

The modal averaged radiation efficiency increases with the increase of structural damping below the critical frequency band. The larger the flow rate, the more significant the effect of structural damping on acoustic radiation efficiency. In the case of low flow velocity, the modal averaged radiation efficiency is not sensitive to the change of structural damping. The structural damping increases from 1 to 4%, and the increase of modal averaged radiation efficiency less than 2 dB. In the case of high flow rate, the modal averaged radiation efficiency will increase by 5 dB when the increment of the structural damping is from 1 to 4%.

Acknowledgements

Thanks to the financial support by the Taishan Scholar Program of Shandong (no. ts201712054).

Conflict of interest

Figures 6–8 in this chapter are reproduced from an AIP Publishing journal paper written by the second and third authors, and all the figures are cited in this text.

According to AIP webpage for Copyright and Permission to Reuse AIP materials, AIP Publishing allows authors to retain their copyrights (<https://publishing.aip.org/>

authors/copyright-reuse). Each Copyright Owner retains the nonexclusive rights to “Reprint portions of the Work (excerpts, figures, tables) in future works created by the Author, in keeping with professional publication ethics”, without obtaining permission from AIP Publishing, and provided clear credit is given to its first publication in an AIP Publishing journal. Any reuse must include a full credit line acknowledging AIP Publishing’s publication and a link to the VOR on AIP Publishing’s site.

Author details


Zhang Xilong¹, Kou YiWei² and Liu Bilong^{1*}

1 School of Mechanical and Automotive Engineering, Qingdao University of Technology, Qingdao, China

2 Key Laboratory of Noise and Vibration Research, Institute of Acoustics, Chinese Academy of Sciences, Beijing, China

*Address all correspondence to: liubilong@qut.edu.cn

IntechOpen

© 2019 The Author(s). Licensee IntechOpen. This chapter is distributed under the terms of the Creative Commons Attribution License (<http://creativecommons.org/licenses/by/3.0>), which permits unrestricted use, distribution, and reproduction in any medium, provided the original work is properly cited. 

References

- [1] Graham WR. Boundary layer induced noise in aircraft, part I: The flat plate model. *Journal of Sound and Vibration*. 1996;**192**(1):101-120. DOI: 10.1006/jsvi.1996.0178
- [2] Graham WR. A comparison of models for the wavenumber-frequency spectrum of turbulent boundary layer pressures. *Journal of Sound and Vibration*. 1997;**206**:541-565. DOI: 10.1006/jsvi.1997.1114
- [3] Han F, Bernhard RJ, Mongeau LG. A model for the vibro-acoustic response of plates excited by complex flows. *Journal of Sound and Vibration*. 2001; **246**(5):901-926. DOI: 10.1006/jsvi.2001.3699
- [4] Liu BL. Noise radiation of aircraft panels subjected to boundary layer pressure fluctuations. *Journal of Sound and Vibration*. 2008;**314**:693-711. DOI: 10.1016/j.jsv.2008.01.045
- [5] Liu BL, Feng LP, Nilsson A, Aversano M. Predicted and measured plate velocities induced by turbulent boundary layers. *Journal of Sound and Vibration*. 2012;**331**(24):5309-5325. DOI: 10.1016/j.jsv.2012.07.012
- [6] Liu BL, Zhang H, Qian ZC, Chang DQ, Yan Q, Huang WC. Influence of stiffeners on plate vibration and radiated noise excited by turbulent boundary layers. *Applied Acoustics*. 2014;**80**:28-35. DOI: 10.1016/j.apacoust.2014.01.007
- [7] Rocha J, Palumbo D. On the sensitivity of sound power radiated by aircraft panels to turbulent boundary layer parameters. *Journal of Sound and Vibration*. 2012;**331**:4785-4806. DOI: 10.1016/j.jsv.2012.05.030
- [8] Cremer L, Heckl M. *Structure-Borne Sound: Structural Vibrations and Sound Radiation at Audio Frequencies*. 3rd ed. Berlin: Springer-Verlag; 1988. pp. 502-505. DOI: 10.1121/1.2060712
- [9] Wallace CE. Radiation-resistance of a rectangular panel. *The Journal of the Acoustical Society of America*. 1972;**51**: 946-952. DOI: 10.1121/1.1912943
- [10] Kou YW, Liu BL, Tian J. Radiation efficiency of damped plates. *The Journal of the Acoustical Society of America*. 2015;**137**:1032-1035. DOI: 10.1121/1.4906186
- [11] Graham WR. The effect of mean flow on the radiation efficiency of rectangular plates. *Proceedings of the Royal Society of London. Series A*. 1998;**454**:111-137. DOI: 10.1098/rspa.1998.0149
- [12] Frampton KD. Radiation efficiency of convected fluid-loaded plates. *The Journal of the Acoustical Society of America*. 2003;**113**:2663-2673. DOI: 10.1121/1.1559173
- [13] Kou YW, Liu BL, Chang D. Radiation efficiency of plates subjected to turbulent boundary layer fluctuations. *The Journal of the Acoustical Society of America*. 2016;**139**: 2766-2771. DOI: 10.1121/1.4949021
- [14] Corcos GM. Resolution of pressure in turbulence. *The Journal of the Acoustical Society of America*. 1963; **35**(2):192-199
- [15] Efimtsov BM. Characteristics of the field of turbulent wall pressure-fluctuations at large Reynolds-numbers. *Soviet Physics Acoustics*. 1982;**28**(4): 289-292
- [16] Smolyakov AV, Tkachenko VM. Model of a field of pseudosonic turbulent wall pressures and experimental-data. *Soviet Physics Acoustics*. 1991;**37**(6):627-631. DOI: 10.1002/chin.200334260

- [17] Williams JF. Boundary-layer pressures and the Corcos model: A development to incorporate low-wavenumber constraints. *Journal of Fluid Mechanics*. 1982;**125**:9-25. DOI: 10.1017/S0022112082003218
- [18] Chase DM. Modeling the wavevector-frequency spectrum of turbulent boundary-layer wall pressure. *Journal of Sound and Vibration*. 1980; **70**(1):29-67. DOI: 10.1121/1.2017510.
- [19] Chase DM. The character of the turbulent wall pressure spectrum at subconvective wave-numbers and a suggested comprehensive model. *Journal of Sound and Vibration*. 1987; **112**(1):125-147. DOI: 10.1016/S0022-460X(87)80098-6
- [20] Howe MS, Feit D. Acoustics of fluid–structure interactions. *Physics Today*. 1999;**52**(12):64-64. DOI: 10.1063/1.882913
- [21] Caiazzo A, Desmet W. A generalized Corcos model for modelling turbulent boundary layer wall pressure fluctuations. *Journal of Sound and Vibration*. 2016;**372**(23):192-210. DOI: 10.1016/j.jsv.2016.02.036
- [22] Hwang Y, Geib F. Estimation of the wavevector-frequency spectrum of turbulent boundary layer wall pressure by multiple linear regression. *Journal of Vibration, Acoustics, Stress, and Reliability in Design*. 1984;**106**(3): 334-342. DOI: 10.1115/1.3269199
- [23] Kou YW. Investigation on sound and vibration characteristics of aircraft plates subjected to aerodynamic loads [thesis]. Beijing: University of Chinese Academy of Sciences; 2016 (in Chinese)
- [24] Nilsson AC, Liu BL. *Vibro-Acoustics*, Vol. 2. Berlin Heidelberg: Springer-Verlag; 2016
- [25] Leppington FG, Broadbent EG, Heron KH. The acoustic radiation efficiency of rectangular panels. *Proceedings of the Royal Society of London. Series A*. 1982;**382**:245-271. DOI: 10.1098/rspa.1982.0100